Atmospheric
Measurement
Techniques

The MUSICA MetOp/IASI H$_2$O and δD products: characterisation and long-term comparison to NDACC/FTIR data

A. Wiegele[1], M. Schneider[1], F. Hase[1], S. Barthlott[1], O. E. García[2], E. Sepúlveda[2,3], Y. González[2], T. Blumenstock[1], U. Raffalski[4], M. Gisi[1,*], and R. Kohlhepp[1,**]

[1]Institute for Meteorology and Climate Research (IMK-ASF), Karlsruhe Institute of Technology, Karlsruhe, Germany
[2]Izaña Atmospheric Research Center, Agencia Estatal de Meteorología (AEMET), Santa Cruz de Tenerife, Spain
[3]Department of Physics, University of La Laguna, Tenerife, Spain
[4]Swedish Institute of Space Physics, Kiruna, Sweden
[*]now at: Bruker Optics GmbH, Ettlingen, Germany
[**]now at: Deutscher Wetterdienst, Offenbach, Germany

Correspondence to: A. Wiegele (andreas.wiegele@kit.edu)

Abstract. Within the project MUSICA (MUlti-platform remote Sensing of Isotopologues for investigating the Cycle of Atmospheric water) ground- and space-based remote sensing as well as in situ data sets of tropospheric water vapour isotopologues are provided. The space-based remote-sensing data set is produced from spectra measured by the IASI (Infrared Atmospheric Sounding Interferometer) sensor and is potentially available on a global scale.

Here, we present the MUSICA IASI data for three different geophysical locations (subtropics, midlatitudes, and Arctic), and we provide a comprehensive characterisation of the complex nature of such space-based isotopologue remote-sensing products. The quality assessment study is complemented by a comparison to MUSICA's ground-based FTIR (Fourier Transform InfraRed) remote-sensing data retrieved from the spectra recorded at three different locations within the framework of NDACC (Network for the Detection of Atmospheric Composition Change).

We confirm that IASI is able to measure tropospheric H$_2$O profiles with a vertical resolution of about 4 km and a random error of about 10 %. In addition IASI can observe middle tropospheric δD that adds complementary value to IASI's middle tropospheric H$_2$O observations. Our study presents theoretical and empirical proof that IASI has the capability for a global observation of middle tropospheric water vapour isotopologues on a daily timescale and at a quality that is sufficiently high for water cycle research purposes.

1 Introduction

Understanding the geological water cycle is essential for predicting weather and climate, where atmospheric water is affected by evaporation, transport, and condensation and strongly interacts with fundamental thermodynamic processes such as energy transport and radiation. But different effects on the energy budget are still not clear such as rainfall evaporation (e.g. Worden et al., 2007) or radiative impacts depending on the present water phase (e.g. Trenberth et al., 2009). Thus, additional knowledge about the water cycle would allow improved weather forecasts as well as more precise climate predictions. Hereby, water vapour isotopologues may give detailed insight into the different processes since the partitioning of the different isotopologues depends on the underlying process (equilibrium condensation or Rayleigh process, ice lofting, mixing of dry and humid air masses, rain evaporation, plant transpiration, etc.). In this paper combined measurements of H$_2$^{16}O and HD^{16}O are used (in the following referred to as H$_2$O and HDO). The enrichment of the heavier isotopologue HDO compared to the main isotopologue H$_2$O is called δD and calculated as a deviation of the ratio of both isotopologues compared to the Vienna standard mean ratio in ocean water (VSMOW).

$$\delta\mathrm{D} = 1000\, ‰ \times \left(\frac{\mathrm{HDO/H_2O}}{\mathrm{VSMOW}} - 1\right) \qquad (1)$$

More than 50 years ago Craig (1961) reported on the measurements of water isotopologues by mass spectrometry in collected liquid water samples from all around the globe. The first atmospheric in situ profiling of water isotopologues in the gas phase was performed by Ehhalt et al. in the 1970s (a review is given in Ehhalt et al., 2005). Since then a few dedicated aircraft campaigns have taken place (e.g. Zahn, 2001; Webster and Heymsfield, 2003) using different in situ instruments. In recent years there has been great progress in remote-sensing observations of water vapour isotopologues. In the meanwhile ground-based FTIR (Fourier Transform InfraRed) instruments (Schneider et al., 2006, 2012) have been used for measuring δD in the lower and middle troposphere. Furthermore, there are space-borne scientific sensors that measure middle tropospheric δD (Worden et al., 2007) and δD at and above the upper troposphere and lower stratosphere (e.g. Steinwagner et al., 2007; Payne et al., 2007; Lossow et al., 2011). Most recently, middle tropospheric δD products applying the operational meteorological satellite sensor IASI (Infrared Atmospheric Sounding Interferometer) have been presented by Schneider and Hase (2011a), Lacour et al. (2012), and Pommier et al. (2014).

These remote-sensing observations are very interesting since they can give a global view on the atmospheric water vapour isotopologues, thus promising unprecedented opportunities for water cycle research on a global scale. However, the remote sensing of trace gas ratios like δD is no trivial task. The trace gas ratio product has rather complex characteristics, and it is important to be aware of these complexities, to understand, and to comprehensively describe them; otherwise its scientific value will be limited.

Such quality assessment is a main objective of the project MUSICA (MUlti-platform remote Sensing of Isotopologues for investigating the Cycle of Atmospheric water, www.imk-asf.kit.edu/english/musica). Schneider et al. (2012) present an extensive theoretical characterisation of the MUSICA ground-based FTIR remote-sensing data set.

In this paper we give a brief overview of MUSICA's NDACC (Network for the Detection of Atmospheric Composition Change)/FTIR and MetOp (Meteorological Operational satellite programme)/IASI products and the applied retrieval strategies (Sect. 2). In Sect. 3 we use the formalism as presented for the NDACC/FTIR data set by Schneider et al. (2012) for characterising MUSICA's MetOp/IASI products. Then, the IASI and the FTIR products are compared in Sect. 4. This is done for three rather different locations: for a subtropical, a midlatitudinal, and a polar site. Sect. 5 concludes the study.

2 Remote sensing of water isotopologues

In the real atmosphere H₂O and HDO vary mostly in parallel: compared to the large variability of tropospheric H₂O and HDO concentrations, the ratio between the HDO and H₂O concentrations remains relatively stable. This is the dominating characteristic of atmospheric water vapour isotopologues and has to be accounted for when setting up a remote-sensing retrieval.

We use the same code (PROFFIT; Hase et al., 2004) for MUSICA's NDACC/FTIR and MetOp/IASI remote-sensing retrievals. In so doing, we want to ensure that the respective ground- and space-based data products are as consistent as possible. The code has been developed and successfully used for the inversion of ground-based absorption spectra as well as thermal nadir spectra (e.g. Schneider and Hase, 2011a). The retrievals are performed in logarithmic scale and with an interconstraint between both water vapour isotopologues. This strategy enables us to account for the dominating characteristics of the atmospheric water vapour isotopologue state.

2.1 The {humidity, δD} proxy state and water vapour isotopologue covariances

The state $\{(\ln[H_2O]+\ln[HDO])/2\}$ captures the large variations that are common to H_2O and HDO, it is a good proxy for H_2O variations, and we refer to it in the following as the {humidity} proxy state. The state $\{\ln[HDO]-\ln[H_2O]\}$ describes the relatively small variations in the HDO/H_2O ratio, it is a good proxy for δD variations, and we refer to it in the following as the {δD} proxy state. The transformation between the $\{\ln[H_2O], \ln[HDO]\}$ state (x) and the {humidity, δD} proxy state (x') can be realised by a transformation matrix $\mathbf{P}$:

$$x' = \mathbf{P}x = \begin{pmatrix} \frac{1}{2}\mathbb{I} & \frac{1}{2}\mathbb{I} \\ -\mathbb{I} & \mathbb{I} \end{pmatrix} x. \tag{2}$$

Here $\mathbb{I}$ is $n \times n$ unity matrix (n is the number of atmospheric grid levels).

This transformation is very useful for defining a correct a priori covariance matrix and thus for setting up the correct constraints for the atmospheric water vapour isotopologue retrievals. For this purpose, we define a matrix $\mathbf{S}_{aH}$, describing the covariances that are common to H_2O and HDO, i.e. the covariances for the {humidity} proxy state. Similarly, we define a matrix $\mathbf{S}_{aI}$ for the {δD} proxy state covariances. These two covariances describe the dominating characteristics of the atmospheric water vapour isotopologue variations.

However, our remote-sensing retrievals work in the $\{\ln[H_2O], \ln[HDO]\}$ state, and to set up an adequate optimal estimation constraint we need to define the a priori covariances for the $\{\ln[H_2O], \ln[HDO]\}$ state. These covariances (represented by $\mathbf{S}_a$) can be easily calculated from the covariances for the {humidity, δD} proxy state (represented by matrix $\mathbf{S}'_a$) by means of the transformation matrix $\mathbf{P}$:

$$\mathbf{S}_a = \mathbf{P}^{-1} \mathbf{S}'_a \mathbf{P}^{-T}$$

$$= \begin{pmatrix} \mathbb{I} & -\frac{1}{2}\mathbb{I} \\ \mathbb{I} & \frac{1}{2}\mathbb{I} \end{pmatrix} \begin{pmatrix} \mathbf{S}_{aH} & 0 \\ 0 & \mathbf{S}_{aI} \end{pmatrix} \begin{pmatrix} \mathbb{I} & \mathbb{I} \\ -\frac{1}{2}\mathbb{I} & \frac{1}{2}\mathbb{I} \end{pmatrix}$$

$$= \begin{pmatrix} \mathbf{S}_{aH} + \frac{1}{4}\mathbf{S}_{aI} & \mathbf{S}_{aH} - \frac{1}{4}\mathbf{S}_{aI} \\ \mathbf{S}_{aH} - \frac{1}{4}\mathbf{S}_{aI} & \mathbf{S}_{aH} + \frac{1}{4}\mathbf{S}_{aI} \end{pmatrix}. \quad (3)$$

For more details please refer to Sect. 3.3 of Schneider et al. (2012), where the {humidity, δD} proxy state is introduced.

2.2 The MUSICA NDACC/FTIR retrievals

The NDACC (http://www.acd.ucar.edu/irwg/; Kurylo and Zander, 2000) FTIR spectrometers measure solar absorption spectra in the mid-infrared region (750–4300 cm⁻¹). The very high spectral resolution (typically 0.0036–0.005 cm⁻¹) allows for observing the pressure-broadening effect in the absorption signatures. As a consequence, the absorption spectra contain some information on the vertical distribution of the absorbing trace gases. For example, in the case of O_3 four independent layers between the surface and about 35 km altitude (Barret et al., 2002; García et al., 2012) and in the case of H_2O three layers between the surface and the upper troposphere (Schneider et al., 2012) can be resolved.

For the MUSICA water vapour isotopologue retrieval, we work with 11 spectral microwindows between 2650 and 3020 cm⁻¹ (see Fig. 2 of Schneider et al., 2012) as well as four spectral auxiliary microwindows containing CO_2 lines (in order to optimally estimate the temperature from the measured spectra; Schneider and Hase, 2008). We use HITRAN 2008 (High-Resolution Transmission Molecular Absorption Database) spectroscopic parameters (Rothman et al., 2009, with 2009 updates), while for the water vapour isotopologues we use parameters that have been adjusted for the speed-dependent Voigt line shape (Schneider et al., 2011b).

We fit simultaneously the spectral signatures of $H_2^{16}O$, $HD^{16}O$, $H_2^{18}O$, $H_2^{17}O$, O_3, N_2O, CH_4, HCl, and C_2H_6. For the constraint of the water vapour isotopologue state we construct a priori covariances for humidity and δD ($\mathbf{S}_{aH}$ and $\mathbf{S}_{aI}$, respectively; see Eq. 3). For humidity, we assume a 1σ variability of 1.0 (on log scale) and a correlation length of 2.5 km throughout the troposphere. For δD, we assume a 1σ variability of 80 ‰ and the same correlation length as for humidity.

For more details about the MUSICA FTIR H_2O and δD retrievals, please see Schneider et al. (2012).

Currently the MUSICA NDACC/FTIR water vapour isotopologue data are available for 10 globally distributed sites (Schneider et al., 2012). In this study we work with three of them that are representative of rather different locations: Izaña at Tenerife Island, Spain (subtropics); Karlsruhe, Germany (midlatitudes); and Kiruna, northern Sweden (polar region).

2.3 The MUSICA MetOp/IASI retrievals

IASI is one instrument aboard the MetOp satellites, which are operated by EUMETSAT (European Organisation for the Exploitation of Meteorological Satellites). Since it flies in a sun-synchronous polar orbit and since IASI measures in a broad scan across the flight path, IASI samples the atmosphere almost everywhere twice a day (morning and evening overpass). IASI is an infrared Michelson interferometer and covers the spectral range from 645 to 2762 cm⁻¹ (3.62 to 15.5 μm). More instrument details can be found at Clerbaux et al. (2009) and August et al. (2012). MetOp-A was launched in October 2006, MetOp-B in September 2012. Here, we only consider spectra measured by the IASI instrument aboard MetOp-A.

For the retrievals, we use a single broad spectral window ranging from 1190 to 1400 cm⁻¹. We fit the $H_2^{16}O$, $H_2^{18}O$, and $H_2^{17}O$ spectral signatures together as a single species and the $HD^{16}O$ as another species. Furthermore, there are spectroscopic features of CH_4 and N_2O, as well as weak spectroscopic features of HNO_3, CO_2, and O_3. All these trace gases are simultaneously fitted during the retrieval process whereby we use the HITRAN 2008 spectroscopic parameters (Rothman et al., 2009, with 2009 updates). We also fit the surface temperature and the atmospheric temperature, whereby the a priori temperatures are the EUMETSAT level 2 temperatures. We put no constraint on the surface temperature, but a very strong constraint on the atmospheric temperature (we only allow for typical variations of 0.25 K, except for the lowermost atmospheric grid point, where we allow for variations of 1 K). We only work with pixels that are declared cloud-free within the EUMETSAT level 2 product. The details of the MUSICA IASI H_2O and δD retrieval setup are described in Schneider and Hase (2011a), whereby for this work we made refinements in two areas.

We now implement emissivity data into the nadir module of the code (please recall that in Schneider and Hase, 2011a, only sea surface pixels are considered and the emissivity is set equal to 1.0): sea surface emissivities are calculated according to Masuda et al. (1988) for three different wavenumbers enveloping the spectral retrieval range and for small wind speeds. This is valid for most of the cloud-free sea surface IASI pixels, since the dependence of the emissivities on the wind speed is weak for small wind speeds and the probability of cloud coverage is enhanced at high wind speeds. Emissivities at land are taken from the Global Infrared Land Surface Emissivity Database provided by the University of Wisconsin in Madison (http://cimss.ssec.wisc.edu/iremis/) as monthly means.

In Schneider and Hase (2011a), we construct a priori covariances for humidity and δD ($\mathbf{S}_{aH}$ and $\mathbf{S}_{aI}$; see Eq. 3) assuming an a priori variability of tropospheric H_2O and δD of 100 and 8 %, respectively, with a correlation length that increases linearly from 2.5 km in the lower troposphere to 10 km in the stratosphere (20 km). For this work we apply a

slightly looser constraint and assume an a priori H$_2$O variability (δD variability) of 75 % (6 %) for the lower troposphere, 150 % (12 %) for the middle and upper troposphere, and 30 % (5 %) for the stratosphere. These values agree reasonably with the simulations made by the model LMDz (Laboratoire de Météorologie Dynamique zoom; see Fig. 2 of Lacour et al., 2012). As correlation length we assume 2 km in the lower troposphere and increase it linearly to 4 km at 10 km altitude and to 8 km in the stratosphere (at 20 km altitude).

3 Characterisation of MUSICA's MetOp/IASI product

Throughout this paper all figures (except for one figure in Sect. 4.3) are subdivided into three parts: to the left for Izaña, representing the subtropics; in the middle for Karlsruhe, representing midlatitudes; and to the right Kiruna, representing polar latitudes.

Figure 1 shows typical kernels for the {ln[H$_2$O]} and the {ln[HDO]} states obtained from the IASI retrievals. As mentioned above, there are three groups of graphs: left group for Izaña, central group for Karlsruhe, and right group for Kiruna. Each group consists of four graphs: the top left and bottom right graphs show how atmospheric ln[H$_2$O] variations affect the retrieved {ln[H$_2$O]} state and how atmospheric ln[HDO] variations affect the retrieved {ln[HDO]} state, respectively. Furthermore, there are large cross-dependencies (top right and bottom left graphs) that have to be considered. They show how atmospheric ln[HDO] variations affect the retrieved {ln[H$_2$O]} state and how atmospheric ln[H$_2$O] variations affect the retrieved {ln[HDO]} state. Due to these cross-dependencies and due to the fact that H$_2$O and HDO vary largely in parallel, a straightforward interpretation of Fig. 1 is difficult.

Much better insight is provided by transferring the {ln[H$_2$O], ln[HDO]} state to the {humidity, δD} proxy state. This proxy state concept enables us to characterise the complex MUSICA MetOp/IASI water vapour isotopologue remote-sensing data by means of the well-known Rodgers formalism (Rodgers, 2000). This is done with great similarity to the characterisation of the MUSICA NDACC/FTIR product as presented in Schneider et al. (2012), to which we refer throughout this section as S12. Very recently Pommier et al. (2014) used the S12 formalism for assessing uncertainties in the IASI water isotopologue product as provided by the Université libre de Bruxelles.

In the following we will characterise the two types of the IASI water vapour isotopologue products.

Table 1. Mean and standard deviation of degree of freedom of signal (DOFs) for the two product types and the three locations.

Location	Product type 1	Product type 2
Izaña	4.15 ± 0.10	0.74 ± 0.10
Karlsruhe	3.78 ± 0.30	0.74 ± 0.20
Kiruna	3.31 ± 0.22	0.57 ± 0.18

3.1 Characterisation of product type 1: optimally estimated H$_2$O profiles

3.1.1 Sensitivity and vertical resolution

The averaging kernel matrix ($\mathbf{A}'$), representative of the {humidity, δD} proxy state, is obtained by a transformation of the {ln[H$_2$O], ln[HDO]} kernel $\mathbf{A}$ (see Eq. 10 of S12):

$$\mathbf{A}' = \mathbf{PAP}^{-1}, \tag{4}$$

whereby the rows of $\mathbf{A}$ are plotted in Fig. 1 and $\mathbf{P}$ is the transformation matrix as defined in Eq. (2).

The rows of kernel $\mathbf{A}'$ are depicted in Fig. 2; i.e. this figure shows the humidity and δD proxy kernels. As in Fig. 1 there are three groups of graphs, representative of the three different locations. The upper left graph of each group documents the sensitivity and vertical resolution of the IASI humidity product (or the H$_2$O product, since H$_2$O and HDO vary largely in parallel). The bottom right graph of each group reveals the sensitivity and the vertical resolution of the IASI δD product. We observe that there is a clear difference between the sensitivity with respect to humidity and δD, meaning that the δD product is sensitive to a different altitude range than the humidity product. Furthermore, the retrieved δD is significantly affected by real atmospheric humidity variations; i.e. it is not independent on atmospheric humidity (see large values in the bottom left graphs of each group).

Product type 1 offers a humidity product with about 4 degrees of freedom for signal (DOFs; see Table 1). It is well suited for investigating the vertical distribution of humidity. However, it is less suited for isotopologue studies, since the δD product has a different sensitivity and is significantly affected by the atmospheric humidity state.

3.1.2 Propagation of uncertainties

The propagation of uncertainties to the humidity and δD states can be calculated as (see Eq. 13 of S12)

$$\mathbf{S}'_\mathrm{e} = \mathbf{PGK}_p \epsilon_p \epsilon_p^T \mathbf{K}_p^T \mathbf{G}^T \mathbf{P}^T, \tag{5}$$

whereby $\mathbf{G}$ is the gain matrix, $\mathbf{K}_p$ the error Jacobian matrix for parameter p, and ϵ_p the parameter uncertainty. We calculate the error Jacobians $\mathbf{K}_p$ as follows: we calculate two
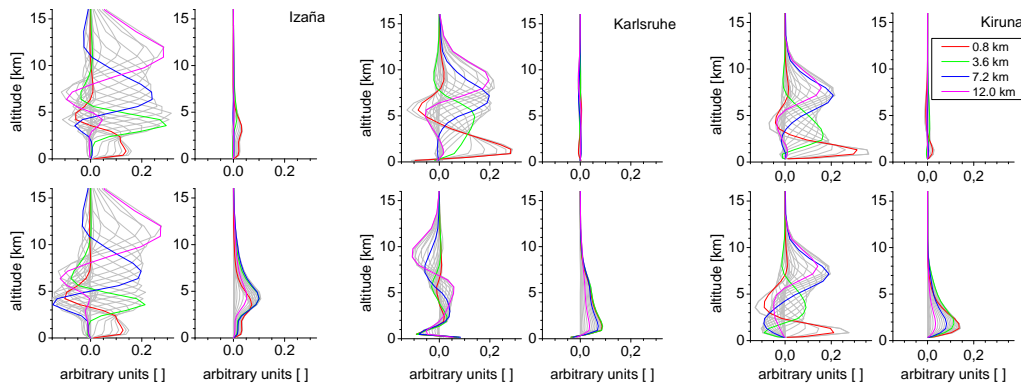
Figure 1. Example of IASI row kernels in the {ln[H₂O], ln[HDO]}-basis (kernel matrix **A**). There are three groups of graphs: left group for Izaña, central group for Karlsruhe, and right group for Kiruna. The upper panels display how the retrieved ln[H₂O] is affected by actual ln[H₂O] variations (left panel of each group) and by actual ln[HDO] variations (right panel of each group). The lower panels display the same for the retrieved ln[HDO].
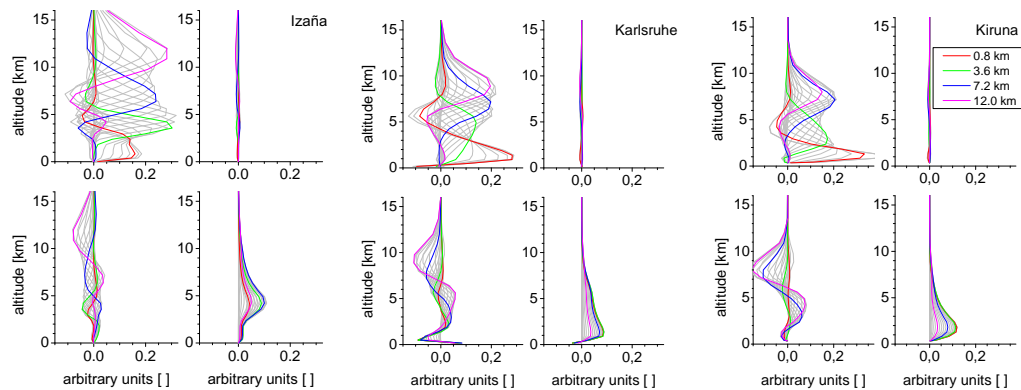
Figure 2. Same as Fig. 1 but for the kernels in the {humidity, δD} proxy state basis (kernel matrix **A′**, Eq. 4). In agreement with Schneider et al. (2012) the cross-correlations are multiplied by the factors 12.5 (lower left panel in each subgraph) and 0.08 (upper right panel).

simulated spectra using a different parameter p. Then we calculate the difference of the simulated spectra and divide it by the difference applied in parameter p.

The assumed uncertainties ϵ_p are listed in Table 2. As measurement noise we assume 5 ‰ (noise-to-signal ratio), which is in agreement with an IASI radiometric noise value of 2×10^{-2} µW/(cm² sr cm⁻¹). This noise value is a rather conservative estimation if compared to the noise level of 4×10^{-3} µW/(cm² sr cm⁻¹) as established by Clerbaux et al. (2009, Fig. 2) for the 1190–1400 cm⁻¹ region. As further instrumental error we assume a small uncertainty in the observation geometry (0.01° uncertainty in the swath angle).

For the line intensity parameters of the water vapour isotopologues (H₂O and HDO) as well as of the major interfering absorbers CH₄ and N₂O, we assume an uncertainty of 2 %. In addition, we consider an uncertainty of the pressure-broadening parameters of H₂O and HDO of 1 %. These assumptions are in good agreement with the uncertainty values given in the HITRAN line lists (e.g. Rothman et al., 2009).

For emissivity we assume an uncertainty value of 5 % (land emissivities are taken from measurements and ocean emissivities from the model of Masuda et al., 1988). In agreement with August et al. (2012), we assume a temperature uncertainty of 2 K for surface temperature and the temperature in the lowermost tropopause (0–2 km) and of 1 K above, whereby we suppose that the uncertainties at ground level and at different atmospheric layers are uncorrelated.

For complex terrain, IASI's ground pixel might cover an area with varying ground altitude. This is considered in our error assessment by assuming an uncertainty in ground altitude of 20 m. In addition, the IASI pixels can be affected by unidentified clouds. This might be low optically thick clouds that only partly cover the IASI pixel (we assume a 5 % coverage) or elevated but optically thin clouds that cover the whole IASI pixel (we assume a cloud with 98 % transmittance).

Figure 3 shows how these uncertainties propagate into the product type 1 humidity profiles. Depicted are the square root values of the diagonal of the error covariance matrix S'_e. The calculations are performed for the three different
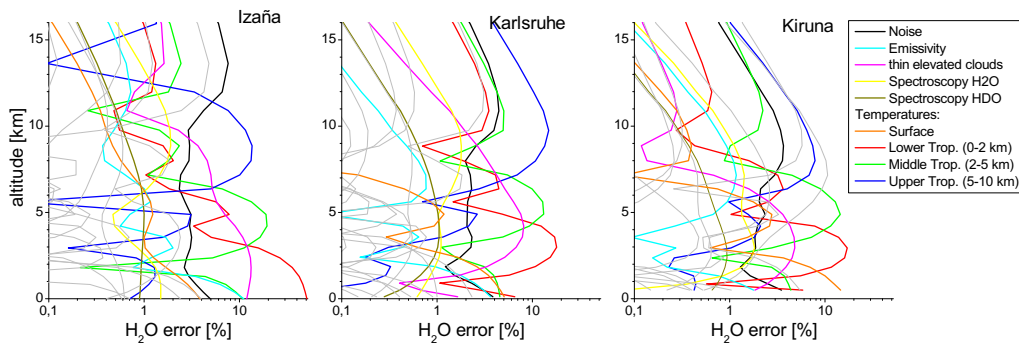
Figure 3. Error estimation for water vapour (product type 1) at all measurement sites. The assumed uncertainty sources are detailed in Table 2. Minor error sources are depicted as grey lines.

Table 2. Uncertainty sources and expected magnitudes used for error estimation of the IASI retrieval.

Uncertainty source	Expected magnitude
Noise	5 ‰
Swath angle	0.01 rad
Line intensity H_2O	2 %
Line intensity HDO	2 %
Line intensity CH_4	2 %
Line intensity N_2O	2 %
Pressure-broadening H_2O	1 %
Pressure-broadening HDO	1 %
Emissivity	5 %
Surface temperature	2 K
Atmospheric temperature (< 2 km)	2 K
Atmospheric temperature (2–5 km)	1 K
Atmospheric temperature (5–10 km)	1 K
Atmospheric temperature (> 10 km)	1 K
Ground altitude	20 m
Cloud at 1 km (optically thick)	5 % cloud coverage
Thin cloud at 10 km	Transmittance 98 %

sites individually (from the left to the right: for pixels measured over the subtropical ocean around Izaña, for land pixels measured around Karlsruhe, and Kiruna). For each site a single and representative typical situation is chosen. All of this situations are measurements during morning overpasses in springtime and have an identical satellite zenith angle of about $25.3°$.

Above the lower troposphere (above 2–3 km altitude), the propagation of the uncertainties is very similar at the different sites. Atmospheric temperature, thin elevated clouds, and measurement noise (in the upper troposphere) are the dominating uncertainty sources. Atmospheric temperature and measurement noise are mainly random uncertainty sources, and we can estimate the random error for the middle/upper tropospheric humidity type 1 product to be about 10 %. The thin elevated clouds occur randomly but also introduce a systematic bias.

In the lower troposphere we predict larger errors for the subtropical ocean scene around Izaña than for the continental scenes around Karlsruhe and Kiruna. This is due to the relatively lower thermal contrast encountered over the ocean as compared to the continent. The surface and boundary layer temperatures for the subtropical ocean around Izaña are about 290 and 291 K, respectively; i.e. there is no thermal contrast between surface and atmosphere. At the continental sites there is significant thermal contrast: at Karlsruhe the temperatures are 290 and 276 K for the surface and the boundary layer temperature, respectively, and at Kiruna it is 279 and 270 K, respectively.

The most important systematic uncertainty source as listed in Table 3 is the spectroscopic parameters. For our assumptions of a 2 % uncertainty in the line intensity and a 1 % uncertainty in the line pressure broadening parameters, we estimate a systematic error in the product type 1 H_2O profile of 2 %.

3.2 Characterisation of product type 2: consistent H_2O and δD data

As outlined in Sect. 4.2 of S12, we have to perform an a posteriori processing in order to ensure that the product can be used for water vapour isotopologue research. This a posteriori processing takes care that the humidity and δD product become sensitive to very similar altitude ranges, and it reduces the dependency of the retrieved δD values on atmospheric humidity variations. The a posteriori processing is realised by a simple matrix multiplication (see Eq. 20 of S12):

$$\hat{x}^* = P^{-1}CP(\hat{x} - x_a) + x_a. \tag{6}$$

Here $\hat{x}$ is the retrieved $\{\ln[H_2O], \ln[HDO]\}$ state, $\hat{x}_a$ the a priori state, and $\hat{x}^*$ the a posteriori corrected $\{\ln[H_2O], \ln[HDO]\}$ state. The matrix P is the transformation matrix of Eq. (2) and C the correction operator (for the definition of C please refer to Eq. 14 of S12).

3.2.1 Sensitivity and vertical resolution

The a posteriori corrected kernel for the {humidity, δD} proxy state is (Eq. 15 of S12)

$$\mathbf{A}'' = \mathbf{CPAP}^{-1}. \tag{7}$$

The rows of $\mathbf{A}''$ are depicted in Fig. 4. The correction has the desired effects. First, it reduces the cross-dependency of humidity on δD (compare bottom left graphs of each group in Figs. 2 and 4), thereby minimising the dependency of the δD product on atmospheric humidity. Second, it assures that the humidity (or H$_2$O) product and the δD product represent very similar altitude regions (compare upper left and bottom right kernels of each group in Figs. 2 and 4). This is important since the added value of δD has to be investigated together with H$_2$O in the form of H$_2$O-versus-δD plots, meaning that both products have to be used and have to be representative of the same altitude regions.

This product type 2 is well suited for atmospheric water isotopologue research. It has a sensitivity that is limited to the middle troposphere (between 2–8 km altitude) and offers typically about 0.7 degrees DOFs (see right column of Table 1).

3.2.2 Propagation of uncertainties

The propagation of the uncertainties can be calculated by (Eq. 19 of S12)

$$\mathbf{S}''_\mathrm{e} = \mathbf{CPGK}_p \epsilon_p \epsilon_p^T \mathbf{K}_p^T \mathbf{G}^T \mathbf{P}^T \mathbf{C}^T. \tag{8}$$

Figure 5 shows how the uncertainties propagate into the type 2 products of H$_2$O (upper panels) and δD (bottom panels). The typical random error for H$_2$O is 3–10 % and is dominated by the atmospheric temperature uncertainties and by not well identified thin elevated clouds. The H$_2$O errors are a bit larger for Izaña than for the other two locations. This is due to the fact that over the subtropical ocean there is a better sensitivity with respect to δD than for the midlatitudinal or polar land scenes. Reducing the H$_2$O sensitivity to the low δD sensitivity also reduces the sensitivity with respect to uncertainties (at Karlsruhe and Kiruna more than at Izaña; compare the groups of kernels in Fig. 4).

The δD error is clearly dominated by the dependency on atmospheric humidity. One and the same atmospheric δD value is observed by IASI with an uncertainty of more than 40 ‰ when observations are made for different atmospheric humidity scenarios (dry versus humid conditions). If there are independent H$_2$O measurements available, we can simulate this error by means of the averaging kernel (bottom left graphs of each group in Fig. 4) and eventually correct it. Please note that this error is even larger if we do not apply the a posteriori correction. Furthermore, measurement noise and thin elevated clouds are important and can sum up to a random error of 15–25 ‰.

The systematic errors due to the assumed spectroscopic line parameter uncertainties are about 1–2 % for H$_2$O and 15–20 ‰ for δD. Further systematic errors might occur in the case of frequently not identified thin elevated clouds.

3.3 Summary of the product characterisation

The IASI water vapour isotopologue products are rather complex and we can offer two different product types. The same classification has been used for the MUSICA NDACC/FTIR data set as presented in Schneider et al. (2012). Type 1 is a water vapour profile product given by the direct retrieval output $\hat{\boldsymbol{x}}$. It is characterised by a good vertical resolution (the respective kernels are depicted in the top left graph in Fig. 2). Type 2 is a product for water vapour isotopologue research and is calculated from the retrieval output by the a posteriori processing as described in Eq. (6). For type 2 the water vapour profile has reduced vertical resolution, but it is representative of the same altitudes as the retrieved δD (the kernels are presented in the top left and bottom right graph in Fig. 4). Furthermore, for type 2 the retrieved δD values are less dependent on atmospheric humidity if compared to retrieved type 1 δD values.

4 Intercomparison of MUSICA's NDACC/FTIR and MetOp/IASI products

In this section we compare the MUSICA MetOp/IASI and the MUSICA NDACC/FTIR water vapour isotopologue remote-sensing products. We do this for product type 1 – the vertically resolved H$_2$O profiles – and product type 2 – the consistent H$_2$O and δD data. In order to facilitate this comparison exercise, both the ground-based FTIR and space-based IASI retrievals use the same a priori profiles for H$_2$O and δD.

4.1 Coincidence criteria

We define that IASI measurements are coincident with FTIR measurements if the time lag is less than 2 h. The spatial criterion is fulfilled if the location of the IASI ground pixel is within a box of approximately 110 km × 110 km bounding the location of the corresponding FTIR instrument to the south. The shift to the south is performed since the FTIR measurements are pointing southward towards the Sun.

We tried to qualitatively assess the validity of these coincidence criteria. For this purpose we use the variation as seen in the FTIR data for estimating the temporal inhomogeneity, and the variations as seen in the IASI data for estimating the spatial inhomogeneity. The scatter (1-σ standard deviation) in the FTIR data observed during the 2 h around local noon are due to FTIR random errors and temporal variations in the atmosphere. We can use it as an upper limit of the temporal inhomogeneity. Similarly we use the scatter between the IASI data corresponding to all morning overpass pixels
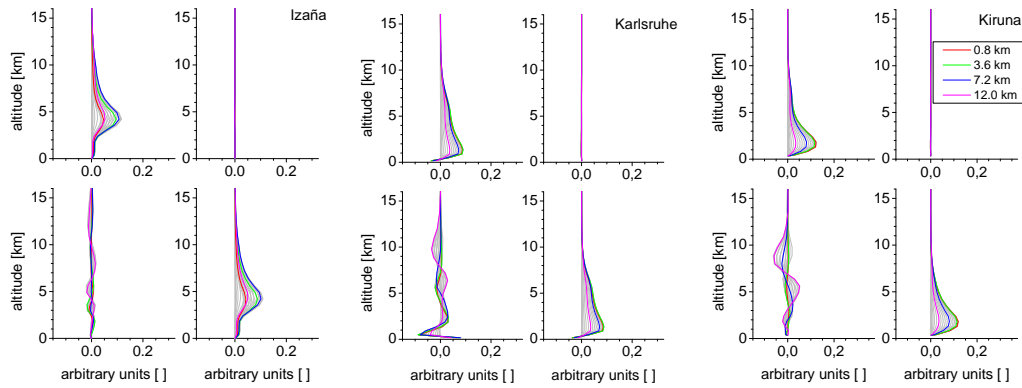
Figure 4. Same as Fig. 2 but for the a posteriori corrected {humidity, δD} proxy state (kernel matrix $\mathbf{A}''$ according to Eq. 7).
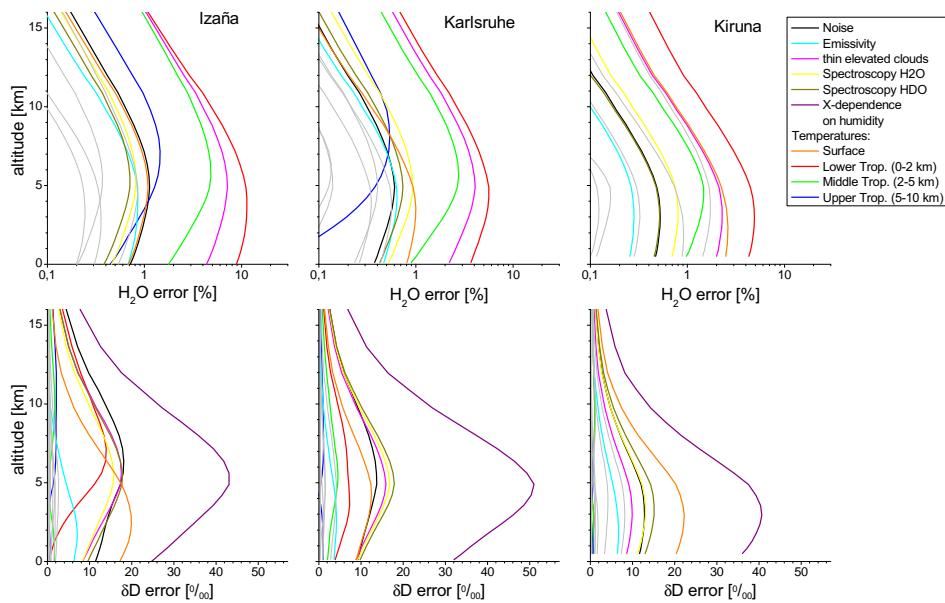
Figure 5. Error estimation for humidity and the isotopologue at all measurement sites. The estimated and used magnitudes can be found in Table 2. Minor error sources are depicted as grey lines and are included in the total error.

Table 3. Estimated potential temporal and spatial mismatch.

	H$_2$O [%]	δD [‰]
Temporal	4.1	7.5
Spatial	19.3	17.5

that fall in our validation box as an upper limit of the spatial inhomogeneity (the scatter is due to IASI random errors and inhomogeneity in the atmospheric fields). These inhomogeneity values are resumed in Table 3 and are calculated from all available FTIR and IASI data (not only the coincidence data). They document how a temporal and/or spatial mismatch between the FTIR and the IASI observations can affect our comparison study.

4.2 Comparing two remote-sensing products

The averaging kernels and thus the altitude resolution and sensitivity for the FTIR and IASI products are different. For product type 1 (vertically resolved H$_2$O profiles) the IASI retrieval yields DOFs of about 4 and best altitude resolutions in the middle troposphere. The FTIR products for the Izaña, Karlsruhe, and Kiruna sites have DOFs of about 2.5–3 and show best vertical resolution close to the surface and reasonable sensitivity up to the middle/upper troposphere. For product type 2 (consistent H$_2$O and δD data) the situation is vice versa. There, the FTIR products offer better sensitivity (DOFs of 1.5–1.7) than the IASI product (DOFs of about 0.7).

These differences limit the comparability of the IASI and FTIR remote-sensing products. We can estimate the effect of the different averaging kernels on the comparability:

$$\mathbf{S}_\mathrm{c} = (\mathbf{A}_\mathrm{I} - \mathbf{A}_\mathrm{F})\mathbf{S}_\mathrm{a}(\mathbf{A}_\mathrm{I} - \mathbf{A}_\mathrm{F})^T, \tag{9}$$

where $\mathbf{S}_\mathrm{a}$ is the atmospheric covariance matrix and $\mathbf{A}_\mathrm{I}$ and $\mathbf{A}_\mathrm{F}$ the averaging kernels for the IASI and FTIR products, respectively. As a metric for the comparability of the two instruments, we work with the square root values of the diagonal elements of $\mathbf{S}_\mathrm{c}$ and calculate the ratio with respect to the square root of the diagonal elements of atmospheric covariance matrix $\mathbf{S}_\mathrm{a}$. The obtained value, $\sqrt{\mathrm{diag}(\mathbf{S}_\mathrm{c})}/\sqrt{\mathrm{diag}(\mathbf{S}_\mathrm{a})}$, is informative on the portion of the atmospheric variability that cannot be compared; i.e. it appears as scatter between the FTIR and IASI products although both instruments and retrievals work perfectly and detect the same air mass. If it is 100 %, we cannot compare the products (the kernels are very different); if it is very low, the kernels of both instruments are quite similar.

4.3 H$_2$O profiles (product type 1)

The left graph of Fig. 6 depicts the comparability values $\sqrt{\mathrm{diag}(\mathbf{S}_\mathrm{c})}/\sqrt{\mathrm{diag}(\mathbf{S}_\mathrm{a})}$ for product type 1; i.e. $\mathbf{S}_\mathrm{c}$ is calculated according to Eq. (9) when using the type 1 kernels for IASI and FTIR. Examples of IASI type 1 kernels are shown in Fig. 2 (for typical FTIR type 2 kernels please see Fig. 3b in Schneider et al., 2012). We find that the IASI and FTIR products are well comparable between 2.5 and 8 km, for the subtropical ocean scene around Izaña, and between 0.5 and 5 km, for the continental scenes at Karlsruhe and Kiruna. For these altitudes we estimate $\sqrt{\mathrm{diag}(\mathbf{S}_\mathrm{c})}/\sqrt{\mathrm{diag}(\mathbf{S}_\mathrm{a})} < 40$ %. A comparison for altitudes above 13 km makes little sense, since there both IASI and FTIR sensitivities are rather low and both sensors report mainly the a priori assumptions.

For the coincidences between IASI and FTIR, direct correlations of water vapour are plotted in Fig. 7 for all three FTIR measurement sites and three different altitudes. The altitudes are selected according to the comparability estimations as presented in Fig. 6. The a priori values are depicted as red stars, and the numbers of coincidences (N) and correlation coefficients (R^2) are given in each graph. At Izaña and Kiruna we compare IASI data measured between 2007 and 2012 and at Karlsruhe between 2010 and 2012 (the Karlsruhe FTIR instrument started its operation in 2010). There are several thousand numbers of coincidences, except for Kiruna where the number is smaller due to the lack of FTIR measurements during polar winter.

We find a very good agreement between the two data sets. Both instruments see very consistent deviations from the a priori values. This is especially true for the middle and upper troposphere. At lower altitudes the correlations tend to be slightly weaker. In addition, we find no significant systematic difference between both instruments. The common a priori values (red stars) fit well into the correlated data points.
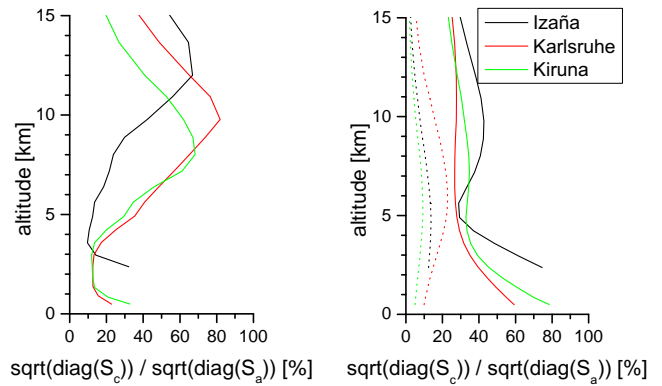
Figure 6. Level of comparability between FTIR and IASI remote-sensing data sets at the three different locations. Left panel: H$_2$O profile product (product type 1), with $\mathbf{S}_\mathrm{c}$ calculations according to Eq. (9). Right panel: consistent humidity and δD data (product type 2), with solid lines representing $\mathbf{S}_\mathrm{c}$ calculations according to Eq. (9) and dashed lines representing $\mathbf{S}_\mathrm{c}^{\mathrm{sm}}$ calculations according to Eq. (10).

The good agreement observed here is consistent with previous studies that compared IASI H$_2$O profile products to meteorological radiosonde data (Pougatchev et al., 2009; Schneider and Hase, 2011a; August et al., 2012).

4.4 Consistent H$_2$O and δD (product type 2)

The solid lines in the right panel of Fig. 6 depict the comparability values $\sqrt{\mathrm{diag}(\mathbf{S}_\mathrm{c})}/\sqrt{\mathrm{diag}(\mathbf{S}_\mathrm{a})}$ for product type 2; i.e. $\mathbf{S}_\mathrm{c}$ is calculated according to Eq. (9) when using the type 2 kernels for IASI and FTIR. Examples for IASI type 1 kernels are shown in Fig. 4 (for typical FTIR type 2 kernels please see Fig. 3c in Schneider et al., 2012). For Izaña these values are smaller than 50 % above 4 km altitude, whereby the respective IASI kernels show maximum sensitivity around 4–5 km altitude (see bottom right panel of Fig. 4), recommending a product comparison around 5 km. For Karlsruhe and Kiruna, the comparability values (solid line in Fig. 6) become smaller than 50 % already above 2 km altitude. In addition, in the Karlsruhe and Kiruna kernels of Fig. 4 we observe that there are IASI sensitivity maxima around 1–3 km; thus, at these two locations a comparison around 2.5 km would be most interesting.

For product type 2 the differences between the IASI and FTIR kernels are larger than for product type 1, whereby the FTIR data offer significantly more DOFs than the IASI data. Under these circumstances we can convolve the FTIR data with the IASI averaging kernels, which modifies Eq. 9:

$$\mathbf{S}_\mathrm{c}^{\mathrm{sm}} = (\mathbf{A}_\mathrm{I} - \mathbf{A}_\mathrm{I}\mathbf{A}_\mathrm{F})\mathbf{S}_\mathrm{a}(\mathbf{A}_\mathrm{I} - \mathbf{A}_\mathrm{I}\mathbf{A}_\mathrm{F})^T. \tag{10}$$

The dotted lines in the right panel of Fig. 6 show the comparability values $\sqrt{\mathrm{diag}(\mathbf{S}_\mathrm{c}^{\mathrm{sm}})}/\sqrt{\mathrm{diag}(\mathbf{S}_\mathrm{a})}$, i.e. with $\mathbf{S}_\mathrm{c}^{\mathrm{sm}}$ calculated according to Eq. (10) and with $\mathbf{A}_\mathrm{I}$ and $\mathbf{A}_\mathrm{F}$ being the
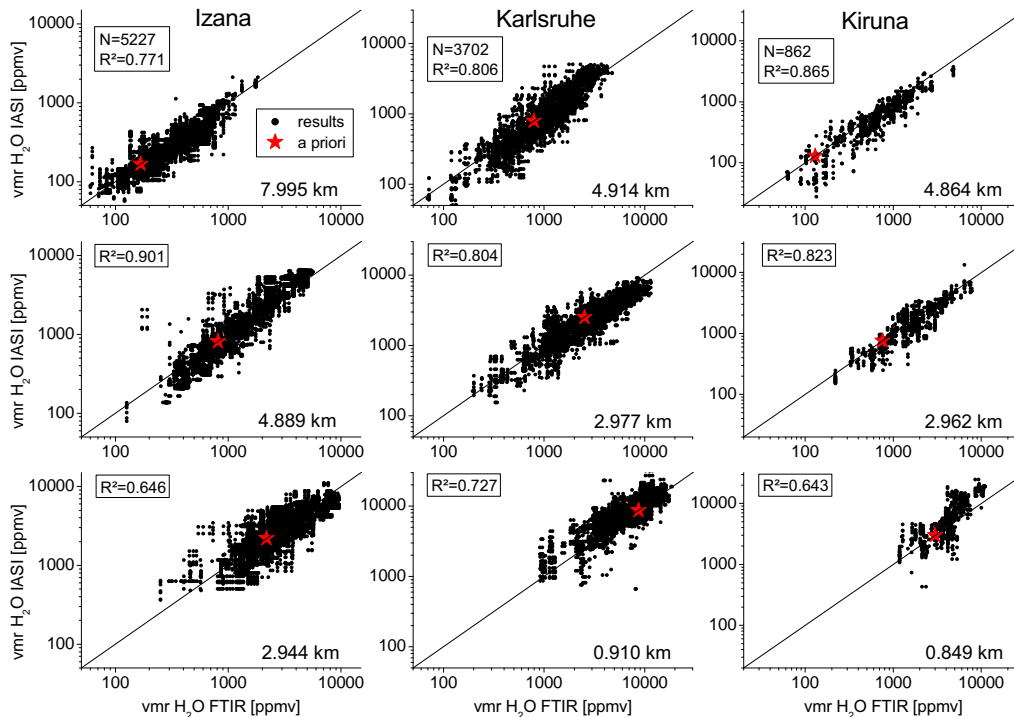
Figure 7. Correlation between the FTIR and IASI H_2O profile data (product type 1) for three different altitudes and the three locations. The chosen levels depend on the altitude range of best comparability (Fig. 6). The a priori mixing ratios are denoted by red stars and the 1-to-1 diagonal is indicated as a black line.
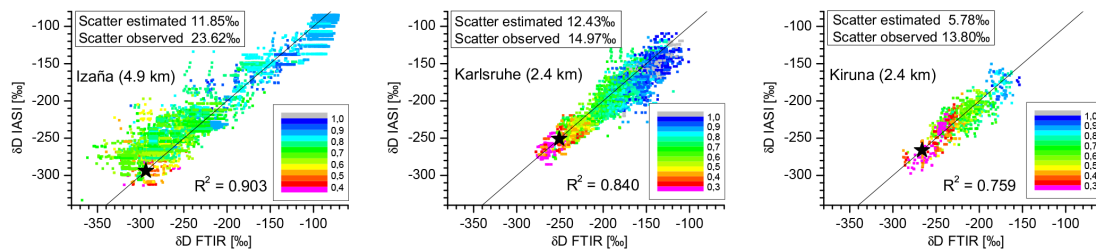

Figure 8. Correlation between the IASI and smoothed FTIR δD data. Colours denote the individual IASI DOFs, the black star marks the a priori, and the black line shows the 1-to-1 diagonal.

type 2 kernels of IASI and FTIR, respectively. The smoothing of the FTIR data with the IASI kernels improves the comparability. Now we get values of about 15 % for the altitudes that are interesting at Karlsruhe and Kiruna (altitudes around 2.5 km) and of about 10 % for 5 km altitude at Izaña.

4.4.1 δD correlations

Figure 8 shows the correlations of the IASI and FTIR type 2 δD products for the three different sites and for the aforementioned interesting altitudes. Here we work with the FTIR product that has been smoothed with the IASI kernels. We find a reasonable agreement and correlation coefficients R^2 of about 0.75–0.90. The graphs demonstrate that IASI and FTIR see very similar atmospheric δD variations.

Furthermore, we observe no significant systematic difference between both data sets (the common a priori values fit well to the correlated data points; see black stars). We observe a scatter between the FTIR and IASI data of less than 15–25 ‰. A part of this scatter is expected to be due to the differences between the IASI and FTIR averaging kernels (values obtained from the calculations according to Eq. (10) are given in the plot as "scatter estimated"). However, most of this scatter is due to errors in the IASI and FTIR data as well as due to a mismatch in the air mass as detected by the IASI and FTIR observations. Assuming negligible errors in the FTIR data as well as no mismatch in the air mass as detected by the FTIR and IASI, we can use this scatter as a conservative estimate of the IASI δD random error. Indeed, the observed scatter of 15–25 ‰ is in very good agreement with our estimations as
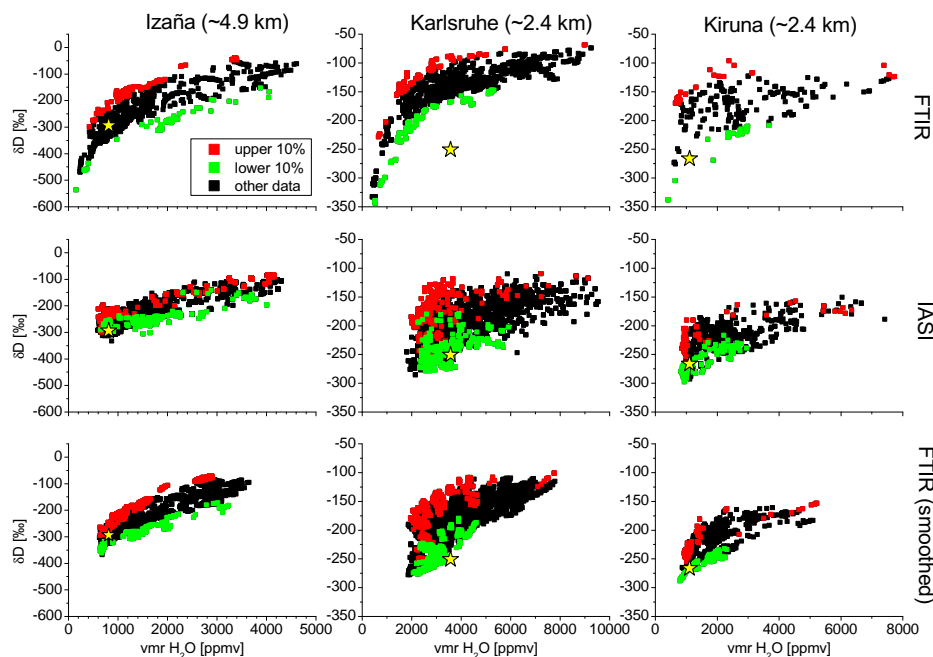
Figure 9. H$_2$O-versus-δD plots for coincident FTIR and IASI measurements for the three locations. Plotted are (from the top to the bottom) the FTIR data, the IASI data, and FTIR data smoothed with the IASI averaging kernels. The colour code displays the upper 10 % and lower 10 % of δD values as identified in the FTIR data. The yellow stars mark the a priori values that are similar for FTIR and IASI.

depicted in the bottom panels of Fig. 5. Please note that the error due to cross-dependence on humidity is an issue of the averaging kernels and its remaining effect on the comparability is accounted for in Eq. (10).

There are several studies that have shown similar correlation plots between δD measurements obtained by two different instruments (e.g. Schneider and Hase, 2011a; Boesch et al., 2013) or between δD measurements and model simulations (e.g. Schneider et al., 2010; Lacour et al., 2012). Such correlations can document that the investigated instrument is able to observe atmospheric δD signals. The lower and middle troposphere is mainly moistened by mixing with a humid air mass and it is dried by mixing with a dry air mass or by condensation. Both processes mean that δD decreases with decreasing humidity, resulting in a strong correlation between H$_2$O and δD. If we observe a decrease or an increase of H$_2$O, a decrease or an increase of δD is very likely. The δD data add scientific value to H$_2$O measurements if we can measure the part of the δD variations that does not follow the typical correlation between δD and ln [H$_2$O]. In this context please see also Sect. 5 of Schneider et al. (2014).

In the following subsection we will examine whether the value added by the IASI δD measurements to the IASI H$_2$O measurements is in agreement with the value added by the FTIR δD measurement to the FTIR H$_2$O measurement.

4.4.2 The added value of δD

For comparing the added value of δD we have to compare δD-versus-H$_2$O plots. Figure 9 shows such plots for Izaña, Karlsruhe, and Kiruna. The upper row shows the data as measured by the FTIR, the middle row the data as measured by IASI, and the bottom row the FTIR data being smoothed by the coincident IASI averaging kernels.

We use the FTIR data of the coincident cases (upper row of graphs) to define strong deviations from the typical δD-versus-H$_2$O curve (i.e. unusual isotopologue observations). The deviations demonstrate that δD observations complement H$_2$O observations. For instance, for an observed H$_2$O concentration we observe δD values not only of -100 ‰ but also of -300 ‰. The low δD (strong HDO depletion) values are likely caused by a prevailing Rayleigh process (the water mass has mainly been dried by condensation and subsequent rainout). The high δD values (weak HDO depletion) suggest mixing of humid and dry air masses or that the evaporation source is a rather cold ocean. Further scientific interpretation of the δD-versus-H$_2$O curves is the subject of future research that will utilise the methods presented here.

In order to identify these deviations, we fit the δD data with a second-order polynomial of ln [H$_2$O]. The red symbols denote the 10 % of all the data that are the most enhanced in δD with respect to the fitted regression curve. The green symbols represent the 10 % of all the data that are the most depleted in δD with respect to the fitted regression curve.

The graphs in the second row also show red and green symbols, which identify the IASI observations that are made in coincidence with the FTIR observations marked with red and green in the upper row of graphs. We find that unusual IASI δD observations strongly coincide with unusual FTIR δD observations. This statement is valid for all three measurement sites.

The graphs in the bottom row show the same as the upper row but for FTIR data smoothed with the IASI kernels. According to the estimations presented in Fig. 6, such smoothing improves the comparability to the IASI data. Indeed, these smoothed FTIR δD-versus-H$_2$O plots agree even better with the respective IASI plots (second row of graphs) than the unsmoothed FTIR curves (upper row).

5   Conclusions

We perform a theoretical and empirical quality assessment study of the MUSICA MetOp/IASI water vapour isotopologue data. We identify two types of products. Type 1 products are vertically resolved tropospheric H$_2$O profiles. Type 2 products are consistent middle tropospheric H$_2$O and δD data and can be used for water vapour isotopologue research.

Our theoretical assessments reveal that the IASI H$_2$O profiles (product type 1) can resolve tropospheric vertical structures of about 4 km; i.e. the full-width half-maximum (FWHM) of the averaging kernels is typically 4 km. The random error of these profile data is generally smaller than 10 %. Only in the lower troposphere can it be a bit larger, in particular for observational scenes with weak thermal contrast (small difference between the surface temperature and the temperature in the lowermost atmospheric layers). The systematic errors due to the assumed uncertainties in the spectroscopic parameters are estimated to be 2 %.

In the middle troposphere IASI can also consistently detect H$_2$O and δD data (product type 2). In order to achieve a consistent product for H$_2$O and δD we need an a posteriori processing. Without this processing there is a high risk of misinterpreting the remote-sensing data due to its high complexity. Without the a posteriori processing the H$_2$O and δD products represent different water mass and the δD product has a significant cross-dependency on humidity. Even despite the a posteriori correction method there remains a cross-dependency on humidity, which can cause δD errors as large as 40 ‰. Beyond this cross-dependency we estimate δD random errors of about 15–25 ‰. For the H$_2$O type 2 product we estimate a random error of 3–10 %.

For our empirical quality study, we use the MUSICA NDACC/FTIR data that correspond to observations that are made in coincidence with IASI overpasses at three different sites. We find that the H$_2$O profiles (product type 1) as observed by FTIR and IASI are in good agreement. This confirms previous studies of IASI H$_2$O profile products.

Good agreement is also found for the H$_2$O and δD product type 2 data. We can prove that IASI detects almost the same middle or lower tropospheric δD variations as the FTIR. Furthermore, the scatter we observe between the two data sets excellently confirms our error estimations.

In order to demonstrate that the IASI and the FTIR δD observations provide consistent scientifically useful information we compare δD-versus-H$_2$O plots. The IASI and FTIR δD-versus-H$_2$O plots of Fig. 9 show that the IASI δD data add information to the IASI H$_2$O measurements and that this added information is in agreement with the information that the FTIR δD data add to the FTIR H$_2$O measurements. This kind of comparison proves that the water vapour isotopologue data produced within MUSICA from MetOp/IASI and NDACC/FTIR observations contain consistent scientifically relevant information. In this context we think that it is important to remark that plotting remote-sensing data on the δD–H$_2$O space, like in Fig. 9, only makes sense if both the retrieved δD and H$_2$O are representative of the same water mass (i.e. only if H$_2$O and δD have more or less the same kernels). This is far from being trivial for remote-sensing data and the paper shows how it can be achieved (a posteriori correction method).

Our study demonstrates the validity of the MUSICA MetOp/IASI water vapour isotopologue data for three rather different geophysical locations: the subtropics, the midlatitudes, and the polar regions. Therefore we conclude that these results provide clear theoretical and empirical proof of IASI's capability for a global observation of lower/middle tropospheric water vapour isotopologues on a daily timescale and at a quality that is sufficiently high for water cycle research purposes.

Edited by: H. Worden

References

August, T., Klaes, D., Schlüssel, P., Hultberg, T., Crapeau, M., Arriaga, A., O'Carroll, A., Coppens, D., Munro, R., and Calbet, X.: IASI on Metop-A: Operational Level 2 retrievals after five years in orbit, J. Quant. Spectro. Radiat. Trans., 113, 1340–1371, doi:10.1016/j.qsrt.2012.02.028, 2012.

Barret, B., De Maziere, M., and Demoulin, P.: Retrieval and characterization of ozone profiles from solar infrared spectra at the Jungfraujoch, J. Geophys. Res. Atmos., 107, ACH 19–1–ACH 19–15, doi:10.1029/2001JD001298, 2002.

Boesch, H., Deutscher, N. M., Warneke, T., Byckling, K., Cogan, A. J., Griffith, D. W. T., Notholt, J., Parker, R. J., and Wang, Z.: HDO/H2O ratio retrievals from GOSAT, Atmos. Meas. Tech., 6, 599–612, doi:10.5194/amt-6-599-2013, 2013.

Clerbaux, C., Boynard, A., Clarisse, L., George, M., Hadji-Lazaro, J., Herbin, H., Hurtmans, D., Pommier, M., Razavi, A., Turquety, S., Wespes, C., and Coheur, P.-F.: Monitoring of atmospheric composition using the thermal infrared IASI/MetOp sounder, Atmos. Chem. Phys., 9, 6041–6054, doi:10.5194/acp-9-6041-2009, 2009.

Craig, H.: Isotopic Variations in Meteoric Waters, Science, 133, 1702–1703, doi:10.1126/science.133.3465.1702, 1961.

Ehhalt, D. H., Rohrer, F., and Fried, A.: Vertical profiles of HDO/H2O in the troposphere, J. Geophys. Res. Atmos., 110, D13301, doi:10.1029/2004JD005569, 2005.

García, O. E., Schneider, M., Redondas, A., González, Y., Hase, F., Blumenstock, T., and Sepúlveda, E.: Investigating the long-term evolution of subtropical ozone profiles applying ground-based FTIR spectrometry, Atmos. Meas. Tech., 5, 2917–2931, doi:10.5194/amt-5-2917-2012, 2012.

Hase, F., Hannigan, J., Coffey, M., Goldman, A., Höpfner, M., Jones, N., Rinsland, C., and Wood, S.: Intercomparison of retrieval codes used for the analysis of high-resolution, ground-based FTIR measurements, J. Quant. Spectr. Radiat. Trans., 87, 25–52, doi:10.1016/j.jqsrt.2003.12.008, 2004.

Kurylo, M. and Zander, R.: The NDSC – Its status after 10 years of operation, Proceedings of the XIX Quadrennial Ozone Symposium, Hokkaido University, Sapporo, Japan, 167–168, 2000.

Lacour, J.-L., Risi, C., Clarisse, L., Bony, S., Hurtmans, D., Clerbaux, C., and Coheur, P.-F.: Mid-tropospheric δD observations from IASI/MetOp at high spatial and temporal resolution, Atmos. Chem. Phys., 12, 10817–10832, doi:10.5194/acp-12-10817-2012, 2012.

Lossow, S., Steinwagner, J., Urban, J., Dupuy, E., Boone, C. D., Kellmann, S., Linden, A., Kiefer, M., Grabowski, U., Glatthor, N., Höpfner, M., Röckmann, T., Murtagh, D. P., Walker, K. A., Bernath, P. F., von Clarmann, T., and Stiller, G. P.: Comparison of HDO measurements from Envisat/MIPAS with observations by Odin/SMR and SCISAT/ACE-FTS, Atmos. Meas. Tech., 4, 1855–1874, doi:10.5194/amt-4-1855-2011, 2011.

Masuda, K., Takashima, T., and Takayama, Y.: Emissivity of pure and sea waters for the model sea surface in the infrared window regions, Remote Sens. Environ., 24, 313–329, doi:10.1016/0034-4257(88)90032-6, 1988.

Payne, V. H., Noone, D., Dudhia, A., Piccolo, C., and Grainger, R. G.: Global satellite measurements of HDO and implications for understanding the transport of water vapour into the stratosphere, Q. J. Roy. Meteorol. Soc., 133, 1459–1471, doi:10.1002/qj.127, 2007.

Pommier, M., Lacour, J.-L., Risi, C., Bréon, F. M., Clerbaux, C., Coheur, P.-F., Gribanov, K., Hurtmans, D., Jouzel, J., and Zakharov, V.: Observation of tropospheric δD by IASI over western Siberia: comparison with a general circulation model, Atmos. Meas. Tech., 7, 1581–1595, doi:10.5194/amt-7-1581-2014, 2014.

Pougatchev, N., August, T., Calbet, X., Hultberg, T., Oduleye, O., Schlüssel, P., Stiller, B., Germain, K. St., and Bingham, G.: IASI temperature and water vapor retrievals – error assessment and validation, Atmos. Chem. Phys., 9, 6453–6458, doi:10.5194/acp-9-6453-2009, 2009.

Rodgers, C. D.: Inverse Methods for Atmospheric Sounding: Theory and Praxis, World Scientific Publisher Co., Singapore, 2000.

Rothman, L., Gordon, I., Barbe, A., Benner, D., Bernath, P., Birk, M., Boudon, V., Brown, L., Campargue, A., Champion, J.-P., Chance, K., Coudert, L., Dana, V., Devi, V., Fally, S., Flaud, J.-M., Gamache, R., Goldman, A., Jacquemart, D., Kleiner, I., Lacome, N., Lafferty, W., Mandin, J.-Y., Massie, S., Mikhailenko, S., Miller, C., Moazzen-Ahmadi, N., Naumenko, O., Nikitin, A., Orphal, J., Perevalov, V., Perrin, A., Predoi-Cross, A., Rinsland, C., Rotger, M., Šimečková, M., Smith, M., Sung, K., Tashkun, S., Tennyson, J., Toth, R., Vandaele, A., and Auwera, J. V.: The HITRAN 2008 molecular spectroscopic database, J. Quant. Spectro. Radiat. Trans., 110, 533–572, doi:10.1016/j.jqsrt.2009.02.013, 2009.

Schneider, M. and Hase, F.: Technical Note: Recipe for monitoring of total ozone with a precision of around 1 DU applying mid-infrared solar absorption spectra, Atmos. Chem. Phys., 8, 63–71, doi:10.5194/acp-8-63-2008, 2008.

Schneider, M. and Hase, F.: Optimal estimation of tropospheric H$_2$O and δD with IASI/METOP, Atmos. Chem. Phys., 11, 11207–11220, doi:10.5194/acp-11-11207-2011, 2011a.

Schneider, M., Hase, F., Blavier, J.-F., Toon, G., and Leblanc, T.: An empirical study on the importance of a speed-dependent Voigt line shape model for tropospheric water vapor profile remote sensing, J. Quant. Spectr. Radiat. Trans., 112, 465–474, doi:10.1016/j.jqsrt.2010.09.008, 2011b.

Schneider, M., Hase, F., and Blumenstock, T.: Ground-based remote sensing of HDO/H$_2$O ratio profiles: introduction and validation of an innovative retrieval approach, Atmos. Chem. Phys., 6, 4705–4722, doi:10.5194/acp-6-4705-2006, 2006.

Schneider, M., Yoshimura, K., Hase, F., and Blumenstock, T.: The ground-based FTIR network's potential for investigating the atmospheric water cycle, Atmos. Chem. Phys., 10, 3427–3442, doi:10.5194/acp-10-3427-2010, 2010.

Schneider, M., Barthlott, S., Hase, F., González, Y., Yoshimura, K., García, O. E., Sepúlveda, E., Gomez-Pelaez, A., Gisi, M., Kohlhepp, R., Dohe, S., Blumenstock, T., Wiegele, A., Christner, E., Strong, K., Weaver, D., Palm, M., Deutscher, N. M., Warneke, T., Notholt, J., Lejeune, B., Demoulin, P., Jones, N., Griffith, D. W. T., Smale, D., and Robinson, J.: Ground-based remote sensing of tropospheric water vapour isotopologues within the project MUSICA, Atmos. Meas. Tech., 5, 3007–3027, doi:10.5194/amt-5-3007-2012, 2012.

Schneider, M., González, Y., Dyroff, C., Christner, E., Wiegele, A., Barthlott, S., García, O. E., Sepúlveda, E., Hase, F., Andrey, J., Blumenstock, T., Guirado, C., Ramos, R., and Rodríguez, S.: Empirical validation and proof of added value of MUSICA's tro-

pospheric δD remote sensing products, Atmos. Meas. Tech. Discuss., 7, 6917–6969, doi:10.5194/amtd-7-6917-2014, 2014.

Steinwagner, J., Milz, M., von Clarmann, T., Glatthor, N., Grabowski, U., Höpfner, M., Stiller, G. P., and Röckmann, T.: HDO measurements with MIPAS, Atmos. Chem. Phys., 7, 2601–2615, doi:10.5194/acp-7-2601-2007, 2007.

Trenberth, K., Fasullo, J., and Kiehl, J.: Earth's Global Energy Budget, Bull. Am. Meteorol. Soc., 90, 311–323, doi:10.1175/2008BAMS2634.1, 2009.

Webster, C. R. and Heymsfield, A. J.: Water Isotope Ratios D/H, ^{18}O/^{16}O, ^{17}O/^{16}O in and out of Clouds Map Dehydration Pathways, Science, 302, 1742–1745, 2003.

Worden, J., Noone, D., and Bowman, K.: Importance of rain evaporation and continental convection in the tropical water cycle, Nature, 445, 528–532, doi:10.1038/nature05508, 2007.

Zahn, A.: Constraints on 2-Way Transport across the Arctic Tropopause Based on O$_3$, Stratospheric Tracer (SF$_6$) Ages, and Water Vapor Isotope (D, T) Tracers, J. Atmos. Chem., 39, 303–325, doi:10.1023/A:1010660001775, 2001.